Flow measurements in microporous media using micro-particle image velocimetry

Xianke Lu, Yuyuan Zhao, and David J. C. Dennis*
School of Engineering, University of Liverpool, Liverpool L69 3GH, United Kingdom

(Received 18 April 2018; published 15 October 2018)

An experimental study focused on the identification of the flow regimes and quantification of the velocity field at pore scale in microporous media is presented and discussed. Transparent porous media are fabricated by removing a pore forming agent in slightly sintered glass beads of size 50 μm between two glass slides, leaving typical pores with a size of 500 μm. Pressure-drop measurements and particle image velocimetry measurements are conducted simultaneously in order to evaluate the flow regimes and flow behaviors at pore size based Reynolds numbers from 0.1 to 140. Four different regimes, pre-Darcy, Darcy, Forchheimer, and turbulent, are found and presented. Spatial distribution and characteristics of the time-averaged velocity in all regimes and fluctuation intensity in transitional and turbulent regimes are investigated. Critical Reynolds numbers are identified using both velocity and pressure-drop measurements and the results agree very well, providing direct evidence underpinning the transition. The effects of porosity on these flow properties are also studied, and finally the flow regime boundaries are compared with the literature. These data provide an insight into the flow properties in microporous media with various porosities and an improved understanding that could be further utilized to enhance the flow and heat transfer performance of microporous media. It also demonstrates that velocity and pressure measurements used in combination can be an effective method for studying microporous media.

DOI: 10.1103/PhysRevFluids.3.104202

I. INTRODUCTION

The transport of fluids through porous media is common in many engineering fields, such as solute diffusion in catalytic reactors in chemical engineering, oil flow in reservoirs in petroleum production, groundwater flow and migration of hazardous wastes in soil in subsurface hydrology, fluid movement in body tissue and blood flow through capillaries in biomedical research, and natural and forced convection in heat exchangers for equipment cooling. However, the understanding of fluid behavior in porous media, especially in microporous media (that can be used for heat transfer applications in electronic devices), is very limited due to the restriction of techniques.

Although some studies have been conducted in the past, the porous media used in most previous studies are limited to packed beds and granular porous media with porosities in the range 0.3–0.5 [1,2], or a typical metal foam consisting of interconnected dodecahedral-like cells with porosity higher than 0.8 [3–5]. And these studies have focused on measuring the average macroscopic

*djcd@liverpool.ac.uk

properties or process variables, such as the porosity, permeability, and pressure gradient [6,7], due to the limitation of measuring technology. However, models have been developed in the past century to characterize the fluid flow in a porous matrix on the basis of macroscopically measurable flow quantities. The first of these models can be traced back to Darcy's publication [8], where he established the well-known Darcy's law that states the relationship between pressure gradient and velocity in porous media. And subsequently, it was modified to include the fluid viscosity and can be stated as follows:

$$\frac{\Delta P}{L} = \frac{\mu}{K} V, \tag{1}$$

where ΔP is the pressure drop, L is the length of the sample, μ is the viscosity of the fluid, K is the permeability of the porous medium, and V is the Darcian velocity of the fluid, which is the volumetric flow rate of the fluid divided by the cross-section area. Unfortunately, Darcy's law is only applicable for very slow moving flows and a quite narrow Reynolds number range. Forchheimer [9] is widely regarded as being the first to extend Darcy's law and suggests a nonlinear relationship between the pressure gradient and fluid velocity. He suggested that, as the velocity of flow increases, form drag becomes more prevalent, and this kind of effect can be accounted for by the addition of the form drag term $\rho C V^2$, where ρ is fluid density and C is a drag coefficient. And then the following quadratic relation was yielded for describing the pressure drop in porous media:

$$\frac{\Delta P}{L} = \frac{\mu}{K} V + \rho C V^2. \tag{2}$$

Recently, Dybbs and Edwards [10] published a comprehensive review paper in which they indicated the existence of four regimes of flow in porous media: (1) the Darcy regime at $\mathrm{Re} < 1$ ($\mathrm{Re} = \rho V d/\mu$, where d is a characteristic length scale of the internal structure of the porous medium, typically the pore diameter), (2) the inertial flow regime which initiates at Re between 1 and 10, and persists to Re of 150, (3) an unsteady laminar flow regime in the range $150 < \mathrm{Re} < 300$, and (4) a highly unsteady and chaotic regime for $\mathrm{Re} > 300$ that qualitatively resembles turbulent flow. In addition, Bear [11] points out the existence of pre-Darcy flow at very low Reynolds number apart from the flow regimes described above. More generally, researchers combined the second and third regimes together, proposing the final four different regimes of flow through porous media as pre-Darcy, Darcy, Forchheimer, and turbulent.

The experimental studies of flow behavior in porous media can be divided into two types. For the first type, studies [1–3,5,12] tried to find out the universal flow regime boundaries in a porous medium by a traditional method such as pressure-drop measurements. These studies treat the porous medium as a black box and measure pressure gradient across them, identifying different flow regimes according to the slope of the $\Delta P/LV - V$ plot. However, most results are unpredictable because, even for the same type of porous medium, the regime boundaries are different from one sample to another. The disagreement should be the result of the various internal structures of porous media, but sometimes it is due to other factors. For instance, using different characteristic length (pore diameter, particle diameter, permeability) based Reynolds number and different calculation methods of permeability both contribute to the disagreement [3]. For the second type of study, experiments are carried out using optical methods for measuring the fluid behavior at the pore scale. These measurement methods make it possible to see how fluid moves through porous media and measure its velocity. Laser Doppler velocimetry (LDV) [13] is one of the earliest effective techniques used to measure the interstitial velocity within porous media. Johnston *et al.* [14] used LDV to measure the fluid velocity in a packed bed consisting of 1.27-cm-diam Plexiglas spheres. However, the single point measurement property of LDV limited its application in collecting the spatial velocity field. Particle tracking velocimetry (PTV) is another technique used by researchers to quantify the fluid velocity field. By using a PTV system, Peurrung *et al.* [15] gave an impressive two-dimensional (2D) vector map in a packed bed with 3.1-mm spheres. Huang *et al.* [16] obtained the 2D and three-dimensional (3D) velocity field and internal porous structure in irregularly packed

TABLE I. Constituent masses and porosities of the samples.

	NaCl (g)	Glass beads (g)	Target porosity	Actual porosity
F72	1.3155	0.8068	65%	72%
F77	1.4167	0.6915	70%	77%
F78	1.4167	0.6915	70%	78%
F81	1.5179	0.5762	75%	81%

7-mm spheres. Particle image velocimetry (PIV) [17] is another widely used technique to probe the instantaneous flow field over 2D or 3D domains. Saleh *et al.* [18] and Northrup *et al.* [19] studied the flow through porous media by using PIV and provided preliminary results of velocity distribution. PIV has been considered the dominant measurement technique for investigating flow behavior in a fluid dynamic field under laminar and turbulent flow conditions in recent years.

All the measurements mentioned above are carried out based on "macro" porous media. Recently, micro-PIV (μ-PIV) has made it possible to quantify fluid velocity in microfluidic devices with spatial resolutions on the order of tens of microns [20,21]. Zerai *et al.* [22] applied μ-PIV to square cross-section throats of widths of 200, 600, and 1000 μm, and obtained the 2D streamline pattern as well as the velocity field. Their experiment gives an insight of fluid behavior in a complex porous matrix. Sen *et al.* [23] packed microglass spheres of size 200 μm inside a glass micromodel, with a typical pore size of 10–50 μm. They studied velocity fields at different spatial locations having different pore structure and found that the statistical distribution of the velocity field agreed well with the available numerical and experimental results pertaining to macroporous media.

In the present work, a μ-PIV system is used to measure the pore scale velocity profile within a microporous medium with a distinctive structure of particular importance for thermal applications. The pressure drop over the porous medium is also measured in order to compare with the previous literature as well as to verify the results obtained by the μ-PIV system. The porous medium is fabricated by removing the pore forming agent in a matrix of packed glass spheres after slight sintering, leaving the same size pores in packed beds. This method breaks the porosity limitations of packed beds and traditional typical metal foams. The porosity of the new porous medium is more controllable from 50% to 85%. The flow is investigated over different porosity samples with different local structure. A very wide range of flow rate is used in order to cover as many fluid regimes as possible. The velocity profile and fluctuation are studied in pore scale. The flow regime boundaries obtained from pressure gradient measurements are compared with that obtained from μ-PIV measurement.

II. EXPERIMENTAL METHODS

A. Preparation of porous media

Porous samples with different porosities were fabricated by the sintering and dissolution process developed by Zhao and Sun [24], as shown in Fig. 1(a). The raw materials used in this work were 50-μm-diam transparent glass spheres (supplied by Richard Baker Harrison Ltd., UK) and 500-μm-diam food grade sodium chloride (which is approximately spherical). During fabrication, sodium chloride powder was mixed with the glass spheres at a prespecified volume ratio according to the target porosity and then compacted in a rectangular mold with two glass slides at the top and bottom. The final porosity is different from the target porosity due to the densification of the glass beads. The final porosity is determined by the volume fractions of the NaCl particles and the interparticle voids in the NaCl/glass beads mixture, less the shrinkage during sintering due to densification. The actual porosity is normally the volume percentage of the NaCl plus $\approx 7\%$. The masses of NaCl and glass beads, along with the target and final porosities, are given in Table I.

The preform was preheated in a low temperature (200–300 °C) furnace first and then moved rapidly to another furnace at 715 °C, sintering for 15 min. The reason for preheating is to avoid

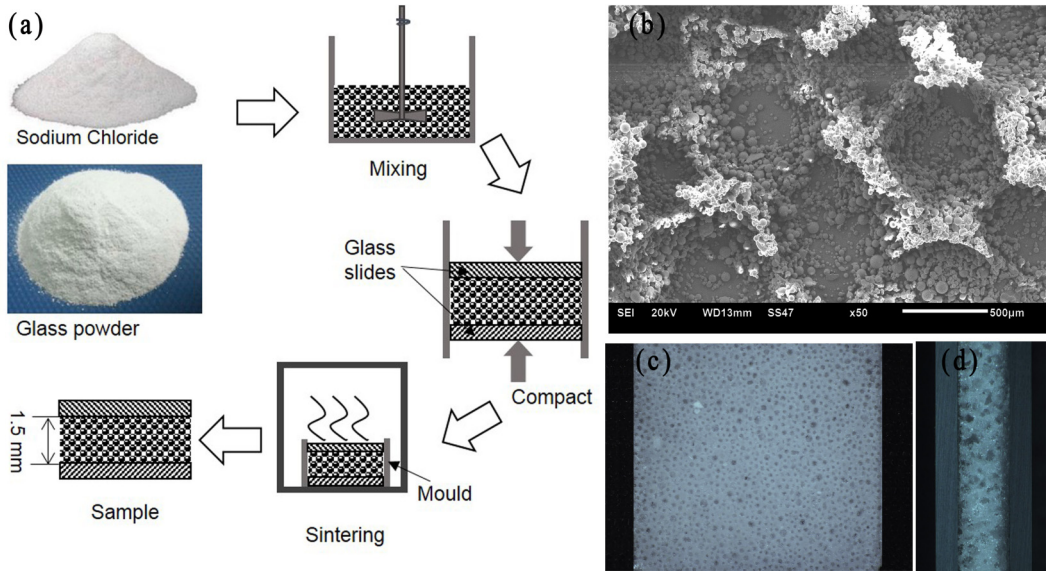

FIG. 1. (a) Fabrication procedure of porous sample. (b) Microstructure of porous medium under scanning electron microscope. (c) Top view and (d) side view of the porous sample.

the burst of the glass due to rapid changes in temperature. For the same reason, after sintering, the sample was gradually cooled to room temperature. Finally, the sample was removed from the mold and the sodium chloride rinsed away in water, leaving an open-cell porous medium with a fixed porosity and pore size.

The surface and typical sandwich structure of the sample, as shown in Figs. 1(c) and 1(d), indicate that pores are distributed very uniformly across the sample. The internal dimensions of the porous structure are $26 \times 25 \times 1.5$ mm^3 (x, y, z), where the thicknesses of the two glass slides are excluded in the z direction. Figure 1(b) shows the typical pore structure in microscale of the porous samples, obtained by scanning electron microscopy (SEM; JSM-6610, Japan). The large pores are negative replicas of the sodium chloride particles and are largely spherical. They are all interconnected to form an open cell network. The cell walls are formed by the sintering of glass spheres and are therefore quite rough. The porosity was determined by measuring the mass of the sample (excluding the glass slides) using an electronic balance and the volume by measuring the dimensions of the sample using a vernier calliper. Then the porosity was calculated as $\epsilon = 1 - \rho_p/\rho_s$, where ρ_p is the density of the porous medium and ρ_s is the density of the solid glass. In the present work, four samples with porosities of 72%, 77%, 78%, and 81% were made under identical conditions, and they are identified as F72, F77, F78, and F81. The accuracy associated with the mass balance was 0.01 g, resulting in an uncertainty in mass of 0.83% for each of the samples. The accuracy associated with the calliper measurements was 0.01 mm, resulting in an uncertainty in length, width, and height of the samples of 0.03%, 0.04%, and 0.28%, respectively. Through a combination of the potential errors in size and mass of the samples, the total uncertainty of porosity was estimated to be 1.21%.

B. Experimental flow rig

In order to create a flow of fluid through the tiny porous sample, a special test rig was designed, as shown in Fig. 2(b). For the purposes of easy machining and light weight when put on the PIV platform, the rig is made of polyvinyl chloride material. The rig consists of a top part and a bottom part. A rectangular channel with internal dimensions of $250 \times 25 \times 1.5$ mm^3 is built on the bottom substrate. To make sure the light from the bottom can be received by the camera, a hole with the

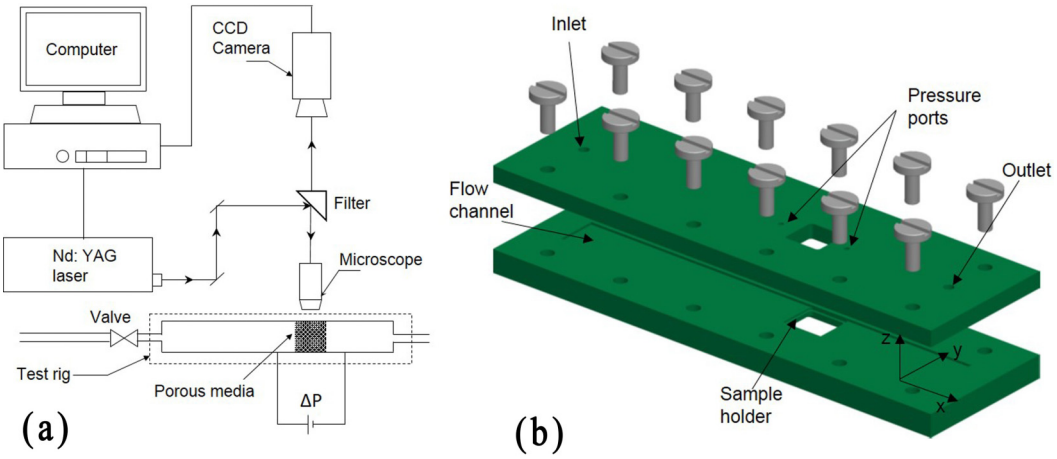

FIG. 2. Experimental setup. (a) A schematic of the micro-PIV facility (not to scale). (b) The exploded view of the test rig (to scale).

same size of the sample was drilled. Steps were machined on both parts at the hole edges so that, on one hand, it is used to hold the sample, and on the other hand, it offsets the thickness of the glass slide. Two ports located 10 mm away from the sample were drilled in both sides and connected with a pressure transducer through pipes. The inlet is 145 mm ($96H$, where H is the height of the channel) away from the porous sample to make sure the flow is fully developed before reaching the porous medium [25,26].

In order to trace the flow path, 1% of the fluorescent particles with diameter of 1 μm (in a liquid suspension state from the supplier) is added to deionized water. Before using water as working fluid, both organic and inorganic solutions were tested to match the refractive index of the porous medium (1.512) so that an optimal view could be obtained, but none of the other fluids worked well in the current setup. Organic solutions such as the mixture of methyl salicylate (1.526) and dimethyl sulfoxide (1.479), with volume ratio of 7:3, and the mixture of benzyl alcohol (1.54) and ethanol (1.36), with volume ratio of 17:3, were tried and the refractive index matches very well. Unfortunately, the organic mixture softened and destroyed all the polyvinyl chloride components (flow rig, pipes, and pressure vessel) and reacted with the fluorescent particles, removing their fluorescence as they could no longer be detected by the camera under laser excitation. Inorganic solutions were also tried, e.g., sodium iodide (1.51, 40 °C, saturated solution) and zinc iodide (1.33–1.62) [27]. The refractive index also matches well, but iodine precipitated gradually from the solution in air and the solution turned to yellow slowly, affecting the image quality significantly. In addition, iodide is quite expensive compared with other candidates. Hence, water was used despite the difference in refractive index compared to the glass (1.33 and 1.512 for water and glass, respectively).

The working fluid (water) is either pumped by a syringe pump (Harvard Apparatus, PHD ULTRA) or driven by pressurized air from a pressure vessel. At low velocity, the syringe pump can control the flow volume rate from 122.2 nl/min to 126.9 ml/min very precisely. When the fluid was driven by pressurized air at high velocity, a mass balance was used to measure the mass flow rate. In order to measure the pressure drop more accurately, three Validyne differential pressure transducer ranges, identified as 0–3.5, 0–22, and 0–140 kPa, were employed across the porous medium.

C. Micro-PIV

The main components of the μ-PIV system (Dantec Dynamics) are shown in Fig. 2. A Nd:YAG laser with a wavelength of 532 nm is used for illumination. The fluorescent particles emit light with

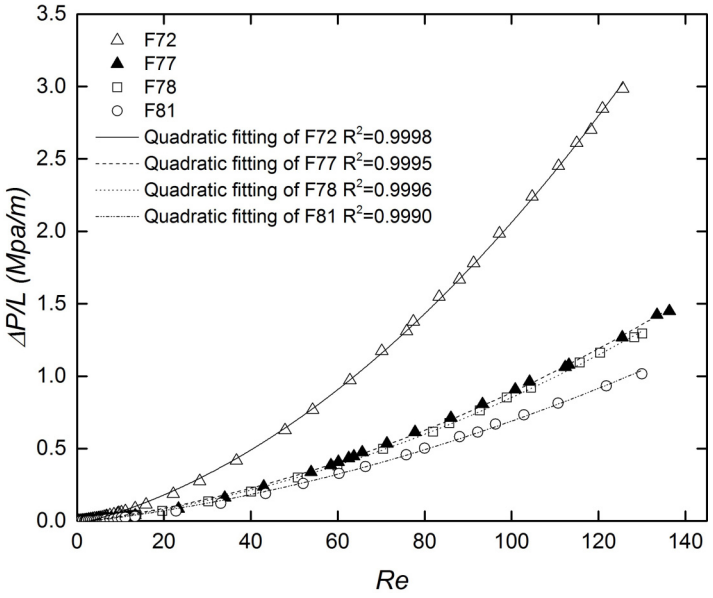

FIG. 3. Pressure gradient versus Reynolds number.

a wavelength of 612 nm when excited by the laser. This long wavelength light from particles reaches the CCD camera, which has resolution of 1600 × 1200 pixels, while the short wavelength light from the remaining parts is filtered out. A 10× microscopic objective, with numerical aperture of 0.25, is used to get an optimum field of view (FOV). The short depth of field of 8 μm is very effective to exclude the particles in adjacent layers and the dimension of the FOV is 800 × 600 μm^2, which fits the pore size very well. The image of a single particle projected on the CCD chip resolves over 2–4 pixels [28]. This can be correctly identified and captured by the analysis software.

For each sample at every chosen Reynolds number, 300 pairs of frames in the xy plane and fixed z position about 250 μm below the porous sample surface, i.e., the center, were acquired. For flow at very low Reynolds numbers (Re < 4), the single frame mode is used to acquire images because under the double frame mode even the maximum time interval is still too short for the flow to move a far enough distance. Under the single frame mode, the time interval between each frame can range from one-tenth of a second to several seconds. In the cross correlations, the adjacent two single frames are treated as a frame pair. For flow at Reynolds numbers larger than 4, the standard double frame mode is used. Under this mode, the time interval between two frames plays a very important role in the PIV measurements. A short interval means a small displacement of particles between two frames, which will magnify the displacement error and thus the velocity error. However, a large time interval may result in particles flowing out of the interrogation area, leading to totally wrong correlations in subsequent cross correlations. In the present experiment, the time interval ranges from 15 to 15000 μs depending on the velocity. DynamicStudio is used to help characterize the flow field by dividing each pair of frames into hundreds of small interrogation areas first, and then a 2D vector map can be obtained by cross correlation of the interrogation cells from the pairs of images.

III. PRESSURE DROP MEASUREMENTS

Figure 3 is a plot of pressure drop over length versus Reynolds number for porous samples. The Reynolds number is defined as $\mathrm{Re} = \rho V D/\mu$, where D is the pore diameter, estimated as being 500 μm, the average diameter of the pore agent (NaCl). The value of permeability and drag coefficient can be obtained by comparing the quadratic curve fitting of the experimental data with

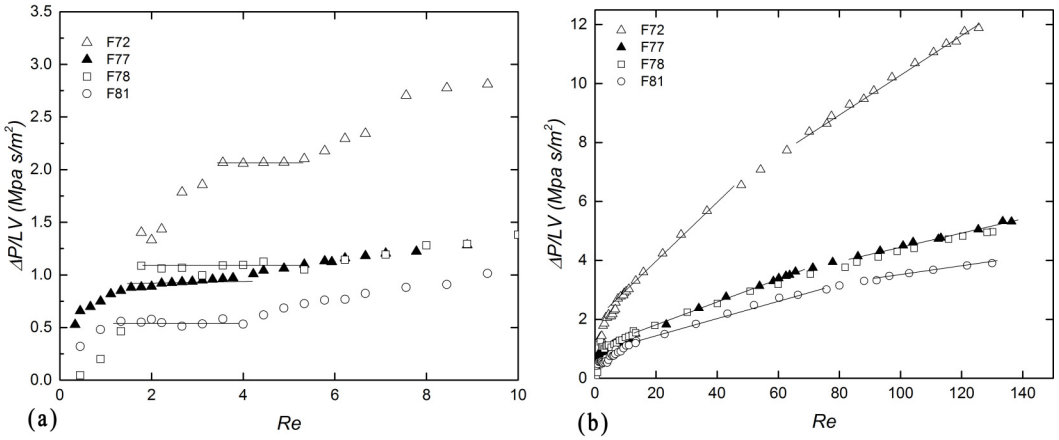

FIG. 4. Pressure gradient versus Reynolds number: (a) pre-Darcy and Darcy regimes and (b) all flow regimes.

Eq. (1) or Eq. (2). The pressure drop in porous media shows a typical quadratic fashion with Re, and the quadratic curve fit of the data shows a very high correlation factor, R^2. For a given Re, the pressure gradient of F72 is more than double that of F77 and F78, which implies the great dependence of pressure drop on porosity.

By dividing Darcian velocity in both sides of Eq. (2), another form can be obtained:

$$\frac{\Delta P}{LV} = \frac{\mu}{K} + \frac{\mu C}{D}\mathrm{Re}. \tag{3}$$

The relationship between $\Delta P/LV$ and Re implies that $\Delta P/LV$ is constant in the Darcy regime because Re is so small that the second term is negligible. In the Forchheimer and turbulent regimes a linear relationship with positive gradient is expected. These flow regimes can be distinguished by slope changes of the curve plotted according to Eq. (3). From Fig. 4(a), the Darcy regime can therefore be identified for each sample at very small Re values. For the present study, Darcy flow occurs at $1 \lesssim \mathrm{Re} \lesssim 5$, and the exact range depends on the pore morphology. The Darcy regime identified is quite different from that identified by Fand *et al.* [1] and Kececioglu and Jiang [2]. The difference can be explained by the fact that they used packed spheres as porous media, which have a completely different internal structure and porosity distribution, and, in addition, the hydraulic diameter used in the Reynolds number was the sphere diameter instead of the pore diameter. The figure also shows that the Darcy regime is quite narrow if compared with other flow regimes in Fig. 4(b). In the Darcy regime, Darcy's law reveals that flow is dominated by viscous forces from the surface of the foam wall. And due to the very low velocity, no inertial cores exist in either the near-wall or the central region of the flow. Thus the flow is only determined and controlled by the actual geometry and internal structure of the foam [10]. We would therefore expect different results for porous samples with the same porosity but produced using different techniques (e.g., packed spheres versus our sintered glass beads) as they would have different pore morphologies. However, two samples produced in the same way, with the same porosity, are expected to give similar results if the pore morphology is reproducible. This is evidenced by samples F77 and F78, which have very similar porosities (actually the same target porosity, see Table I) and give very similar results.

For extremely low velocity, a pre-Darcy regime is identified, as shown in Fig. 4(a). According to previous studies, in the pre-Darcy regime, the increase in fluid velocity can be greater than that proportional to the increase in pressure gradient. Researchers have proposed a number of mechanisms to explain the pre-Darcy phenomena, and among these models the interactions between medium and fluids attracted the most attention. As Polubarinova-Koch [29] pointed out, water has a polar molecule which tends to orient itself in an electrostatic field. Static water molecules can

TABLE II. Permeability and drag coefficient calculated at various flow regimes: K (10^{-10} m^2), C (10^4 m^{-1}).

	Darcy regime	Forchheimer regime		Turbulent regime		All regimes	
	K	K	C	K	C	K	C
F72	5.40	4.04	4.25	2.60	3.32	3.04	3.50
F77	12.1	9.53	1.94	4.76	1.19	5.39	1.29
F78	9.69	8.11	1.64	5.30	1.20	6.15	1.32
F81	18.3	9.92	1.35	5.02	0.75	6.74	0.93

become oriented around surfaces, forming a quasicrystalline structure that effectively narrows the pores or completely occludes them. As an increasing gradient is applied to the water in the porous medium, the weak intermolecular bonds are progressively overcome. In effect, the network of flow channels in the medium becomes a function of fluid velocity. The permeability of the medium increases with fluid velocity until the quasicrystalline water structures are all broken down and Darcy linearity is obtained. Because the behavior of water bound to pore walls by electrostatic force might be considered to be non-Newtonian, some researchers [1,30] attributed the existence of pre-Darcy flow to non-Newtonian behavior of fluids. However, experimental data in this regime are very limited both in the present study and in the literature due to the difficulties in measuring rather small flow rates and pressure drops.

The term non-Darcy normally refers to the combination of Forchheimer regime and turbulent regime. For non-Darcy regimes, in addition to the viscous forces that are solely responsible for Darcy flow, the inertial force and turbulence effects come to play an important role. The near-wall layers developed in the Darcy regime become more and more pronounced [10]. The movement of inertial cores from near-wall layers where they developed to the non-near-wall region cause a nonlinear relationship between the pressure gradient and the flow rate. The relationship can be described by Eq. (2), but with different parameter (permeability and drag coefficient) values. In addition to the inertial force, pore constriction and development of turbulent flow lead to more kinetic energy being degraded, consequently resulting in a decreased permeability. The trend can also be indicated from Fig. 4(b). It shows a decreased slope and increased intercept for the turbulent regime compared to the Forchheimer regime. This means that, according to Eq. (3), both permeability and drag coefficient decrease when the flow transitions from Forchheimer flow to turbulent flow.

Table II shows the permeability and drag coefficient of each sample calculated by two different methods [3]. One method uses the pressure-drop data points from each separate regime without including the transition points; the second method uses a larger flow velocity range which encompasses all the data from the pre-Darcy regime to the turbulent regime. It is noted that the Darcy regime is excluded when calculating the drag coefficient for all regimes. The results in Table II agree with the previous works that investigated the hydraulic characteristics of porous media [31]. It is found that values for the permeability and drag coefficient of the porous medium depend upon the flow regimes over which they are calculated. In other words, permeability and drag coefficient are related to the flow behavior. We speculate that permeability in the Darcy flow regime is much larger because of the weak effects from near-wall layers and low energy dissipation in the flow. In the non-Darcy flow regime, the inertial drag force effects and kinetic energy degradation resulting from pore walls and sharp changes of the flow direction lead to the decrease of mass transfer efficiency. What causes the decrease of drag coefficient from the Forchheimer regime to the turbulent regime is still unclear.

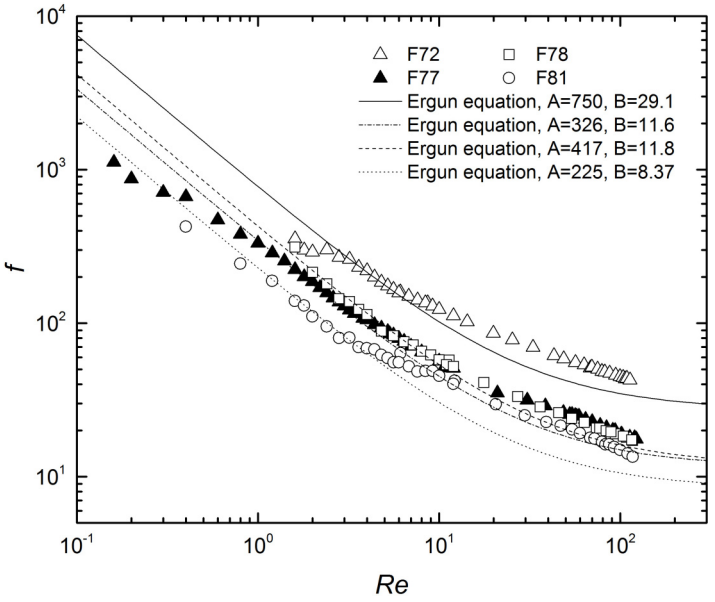

FIG. 5. Pore diameter based friction factor versus pore diameter based Reynolds number in all regimes. Ergun equation is given in Eq. (5).

To improve the understanding of when inertial forces start to make flow deviate from the Darcy flow, the friction factor is extracted by rewriting Eq. (2) as

$$f = \frac{2D^2/K}{\mathrm{Re}} + 2CD, \tag{4}$$

where the friction factor $f = (\frac{\Delta P}{1/2\rho V^2})(\frac{D}{L})$. Based on experimental data for packed bed porous media, Dybbs and Edwards [10] give a more general form (the Ergun equation):

$$f = \frac{A}{\mathrm{Re}} + B, \tag{5}$$

where the values of A and B are highly dependent on the choice of characteristic length for Reynolds number and friction factor. Some researchers [3,5] prefer to use the square root of permeability (especially for the Darcy regime) as the characteristic length. In this case, the value of A should be of order 1 for most porous media. However, from the definition of the Reynolds number point of view, pore diameter is much more appropriate than the square root of permeability to calculate the velocity gradient and thus the viscous force. In addition, permeability is calculated from curve fitting and it changes from one regime to another; as a result, the reliability is much lower than for pore diameter.

Figure 5 shows the friction factor calculated from experimental data curves in the format of Eq. (5). The values of A and B for the curves are calculated according to Eqs. (4) and (5) for each sample. The permeability of the Darcy regime is used to calculate A and the drag coefficient of all regimes is used to calculate B in order to have a better fitting. One may note that the value of A ranges within several hundreds, which is much larger than previous measurements [10,32,33]. This is related to the choice of characteristic length but does not affect the curve trend. Experimental data fit the curve well only in a very narrow Reynolds number range, which should be the Darcy regime. The data start to deviate from the curve slightly in the Forchheimer regime, but due to the limited quantity of experimental data the trend is unclear for high Reynolds numbers. However, the curve reveals that the friction factor tends to be a constant when Reynolds number is larger than the value

of A. Equation (5) also implies this phenomenon because when the Reynolds number gets very high, the first term on the right-hand side of Eq. (5) becomes negligibly small, and thus f approximately equals B. And it is expected that B will be different for different porous media.

IV. MICRO-PIV MEASUREMENTS

The results of all velocity measurements are presented using a Cartesian right-handed coordinate system with the axes in the following directions [Fig. 2(b)]: x = streamwise, y = lateral, z = bed normal, and the corresponding respective velocity components denoted with u, v, w. The time-averaged local velocity magnitude is represented by $\bar{U}$, and the bulk velocity used for normalization of velocity statistics is the Darcian velocity V.

A. Time-averaged velocity distribution in porous media

In order to gain an insight into the details of the flow behaviors in porous media, the velocity fields from the pre-Darcy regime to the turbulent regime in individual pores are studied. Although each sample and region will have unique properties, the flow through different samples behaves similarly and shows an identical trend. To be concise, only one sample, F72, is taken as an example for detailed visual analysis, but we present statistics for all samples tested. Figure 6(a) shows the local porous structure with fluid passing through, and W and H represent the width and height of the field of view. The structure consists of a main pore (pore 1) in the center and another pore (pore 2) in the upper left corner, and a narrow neck region formed due to the overlap of the two pores. The neck region plays a crucial role in connecting neighboring pores and thus forming an open channel network to let fluid pass through from one pore to another. An irregular island protrudes into the neck region, narrowing the flow channel again. For this given local structure, theoretically flow can get into pore 1 only from inlet 1, but can get out from three outlets. Outlet 1 is located in the focus plane, forming an acute angle with the streamwise direction (x direction), while outlet 2 is located deeper than the focus plane in the z direction, forming an apparent right angle with the streamwise direction, and the fluid has to move perpendicularly to the mean flow direction in order to flow out through this outlet. Outlet 3 is a complicated path with three acute angle turns; some parts of outlet 3 are in the focus plane and some parts are not, and therefore to exit through this outlet, the flow needs to move downward first, passing through the solid bridge, and then move upward to the focus plane again. Some other outlets or inlets may exist besides these mentioned above due to the complex structure, but to make the interpretation easier, the geometry is characterized in this simplified manner.

A reference line which is perpendicular to the x direction has been drawn across the pore (the reference line is drawn in all contour plots) and the time-averaged velocity magnitude along the line is plotted in Fig. 6(b). Contour plots of the time-averaged velocity magnitude with vector maps are also presented to give a view of the velocity distribution through the pores. The color indicates the magnitude of velocity and the arrow indicates the direction of local velocity. The solid background is white in contour plots as only noise exists in these regions. For this specific structure, the main flow is divided into two subflows by the island as shown in the contour plots. To make it easier to describe, the flow is divided into three regions, identified as region 1, region 2, and region 3. Normally, the velocity should decrease to zero from the center of a pore to the near-wall region because of the friction effect from the pore wall (no slip condition). However, in reality, the PIV measurement error at the near-wall region is high because when fluid passes along the wall, the fluorescent particles tend to stick on the irregular glass surface of the rough wall, resulting in a very bright fringe, making it very difficult to precisely trace the path of the particles. Therefore, some points are missing in the near-wall region in Fig. 6(b).

The variation in velocity magnitude with Reynolds number is apparent in both the velocity profile figure and the contour plots. In the pre-Darcy regime (Re = 0.2), the maximum velocity magnitude in region 1 is about two times higher than that of region 3 as the curve shows in Fig. 6(b). The vector

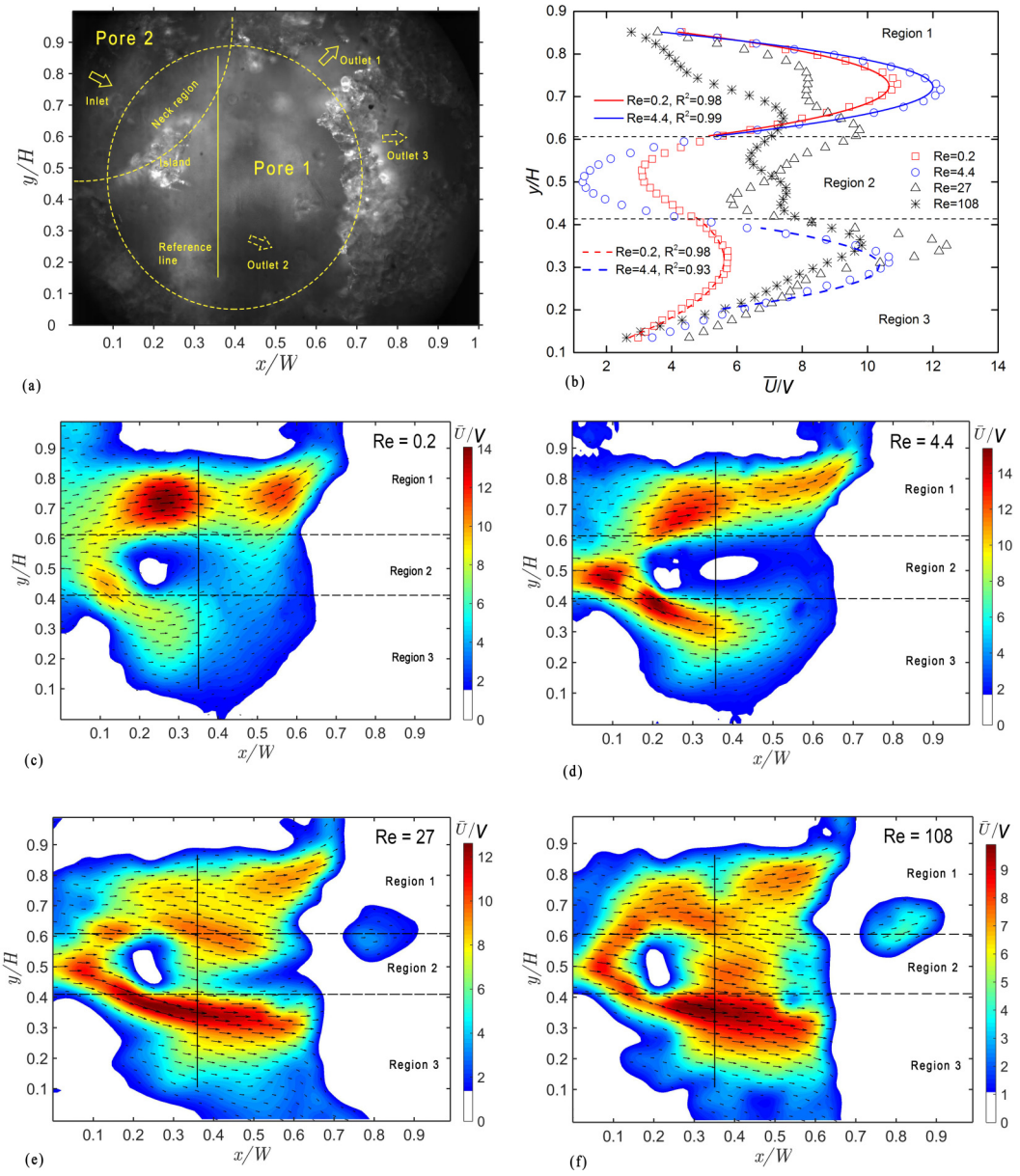

FIG. 6. Velocity profile in a pore of F72 at various Reynolds numbers. The color represents the magnitude of the velocity, and arrows represent the time-averaged velocity directions. (a) Pore structure, (b) velocity profile along the reference line in (a) at different flow regimes, (c) pre-Darcy flow regime, (d) Darcy flow regime, (e) Forchheimer flow regime, and (f) turbulent flow regime.

map in Fig. 6(c) shows that all the fluid tends to get out of pore 1 through outlet 1 as even the flow in region 3 moves toward outlet 1. The velocity data are fitted with a parabolic function separately in region 1 and region 3, and both of them show a very high correlation factor R^2. Apparently, the flow in the pore approximates to a fully developed laminar flow profile in the pre-Darcy regime.

At a Reynolds number about 20 times higher (Re = 4.4), in the Darcy flow regime, the velocity profile has the same trend with that in pre-Darcy regime, but there are also some differences.

Although the normalized velocity has increased in both region 1 and region 3 (in comparison with pre-Darcy flow), the normalized velocity in region 3 has increased much more and the maximum value becomes comparable with that of region 1. The normalized velocity in region 2 has decreased and is much lower than that in the pre-Darcy regime. The low velocity in region 2 means less fluid is transported from region 3 to outlet 1 and is explained by fluid in region 3 flowing out of outlet 2. The vector map in Fig. 6(d) reinforces this conclusion as the velocity in region 2 is almost zero (meaning no flow there), and nearly all the vectors in region 3 point in the x direction. Since outlet 2 locates deeper than the focus plane, the fluid has to move in the negative z direction in order to exit from outlet 2. We propose that when the Reynolds number reaches a certain value, the higher momentum fluid can overcome the resistance in the directions which have a large angle to the streamwise direction, and the velocity component v and w start to increase. The data in region 1 still fit very well to a parabolic; however, the data in region 3 deviate from this shape. The deviation may be attributed to the commencement of fluid flow in the z direction, which is not measured by μ-PIV. Despite this change, the flow is still laminar. Compared with the pre-Darcy regime, channels which have large angles to the streamwise direction become involved in fluid transport in the Darcy regime; i.e., new flow paths are opened. And the difference of the flow path through porous media may account for the pressure gradient difference between the pre-Darcy regime and the Darcy regime in Fig. 4(a).

For flow in the Forchheimer regime, shown in Fig. 6(e), the normalized velocity in region 3 has increased again and exceeds the velocity in region 1 as the velocity in region 1 has decreased significantly. Some fluid in region 1 flows out from outlet 1 and some flows out from outlet 3 and even outlet 2, which effectively makes the channel wider than before, and leads to the decrease of the velocity peak in region 1. Compared with the velocity distribution of region 2 in the pre-Darcy regime, the mean velocity direction is changed completely from the pre-Darcy regime to the Forchheimer regime. In the pre-Darcy regime, the flow direction is from region 3 to outlet 1 (upward), while in the Forchheimer regime, the flow direction is from region 1 substantially directed towards outlet 2 or outlet 3 (downward). The normalized velocity increases from the Darcy regime to the Forchheimer regime in region 2 also because the fluid in region 1 starts to pass through region 2 and flows out from outlet 3, but a region with low velocity still exists downstream of the island in region 2. The velocity profile in both regions is far away from the parabolic fashion.

The velocity profile in the turbulent regime, as shown in Fig. 6(f), is similar to that in the Forchheimer regime, but the velocity becomes significantly more uniform along the line as well as over the pore. The velocity magnitude in region 2 becomes comparable with the other two regions, and the mean velocity direction becomes more parallel with the x direction than in the other three regimes. All these phenomena may be caused by turbulence which transports the momentum more efficiently throughout the pore.

As listed in Table II, the permeability changes from one regime to another; therefore, the regime in which the permeability represents the true property of the materials is debated among researchers. Some researchers [5,10] prefer Darcy permeability as the actual permeability of porous media, because in the purely viscous Darcy regime, the exact nature of the flow field was determined by the local internal geometry of the porous media. However, in our μ-PIV measurements, the channels between pores that are involved in the transport of the fluid are different with different regimes. It implies that the permeability peak may exist around the Darcy regime and a different permeability should be used according to the regime.

B. Velocity fluctuations in porous media

Figure 7 shows an example of the velocity fluctuation in the Forchheimer [Fig. 7(a)] and turbulent [Fig. 7(b)] flow regimes. In arriving at these results, the local mean velocity components $\bar{u}$ and $\bar{v}$ were subtracted from each velocity record respectively, and then the velocity fluctuation was normalized by the local time-averaged velocity magnitude, $\overline{U}$. The local fluctuation intensity is defined as $U' = \sqrt{(u'_{rms})^2 + (v'_{rms})^2}/\overline{U}$, where u'_{rms} and v'_{rms} are fluctuations of the velocity. In order to remove the effects of unreasonable correlations and experimental errors, the background is

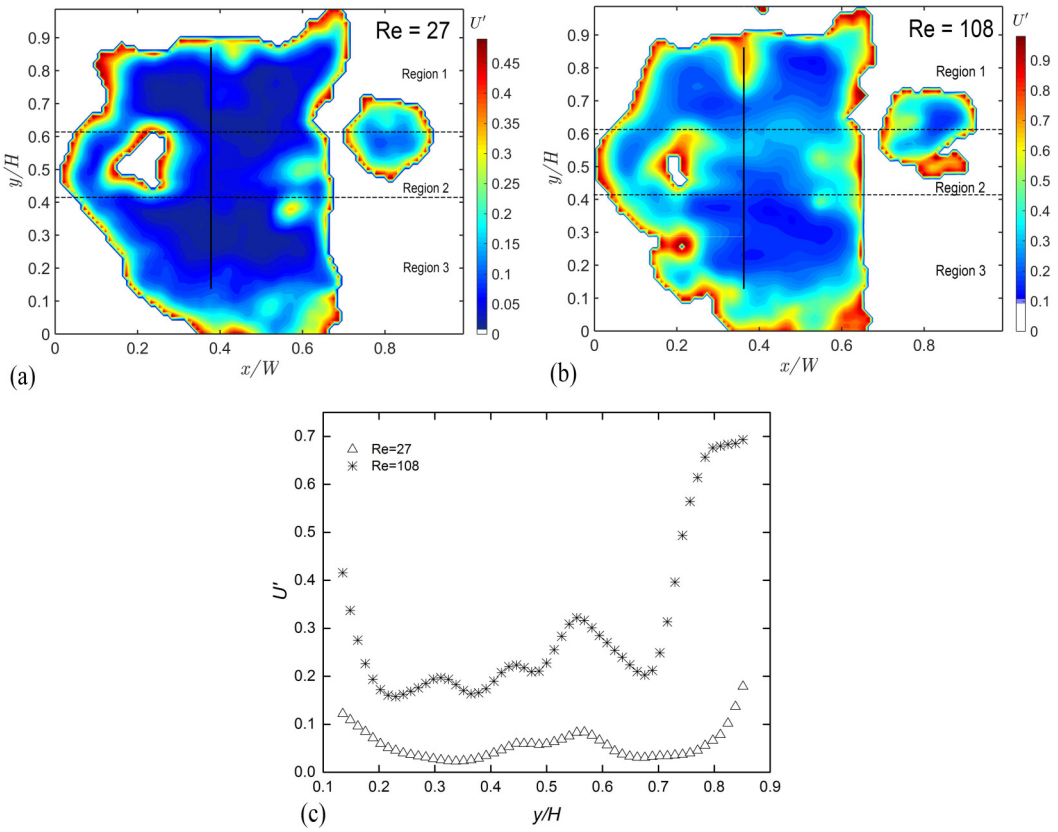

FIG. 7. Velocity fluctuation intensity in a pore of F72 at different Reynolds numbers. (a) Re = 27 (Forchheimer regime), (b) Re = 108 (turbulent regime), and (c) fluctuation intensity along the reference line.

set to be white. It can be seen that when Re = 27, the fluctuation intensity in most regions of the pore is less than 10%. Conversely, when Re = 108, the fluctuation intensity is higher than 10% all over the pore. Actually, when Re = 108, the intensity is larger than 15% in all regions and larger than 20% in most regions of the pore. The contour maps also clearly show that the velocity fluctuation intensity decreases gradually from the near-wall region to the pore center. The high fluctuation intensity in the near-wall region can be attributed to two reasons. First, the rough surface of the pore wall intensifies the fluctuating motion of the fluid. Second, as the local mean velocity magnitude ($\bar{U}$) near the wall is quite small due to viscous effect, the fluctuations will appear large when normalized by this low value. In addition, the fluctuation intensity in region 2 is significantly higher than in the other two regions. This is a region that contains the wake of the island identified in Fig. 6(a). It is therefore a region where the two streams from regions 1 and 3 are interacting and mixing, leading to this increased level of fluctuation.

Fluctuation intensity along the reference line in the turbulent regime is shown in Fig. 7(c). Intensities of the flow in the Forchheimer regime (Re = 27) were also presented for comparison. The figure shows a large difference between the two flow regimes, as the overall intensities at Re = 108 are about three times higher than the intensities at Re = 27. The PIV measurement has verified that the flow in the Forchheimer regime is not turbulent, but unsteady laminar flow (vortices appear at fixed positions, and most of the local velocity in the whole vector map changes direction only slightly with time); after the Forchheimer regime, the flow becomes more unsteady and chaotic, qualitatively resembling turbulent flow. Compared to a simple wall-bounded flow, in porous media the turbulence intensities do not show any clearly defined shape, beyond that of high fluctuations

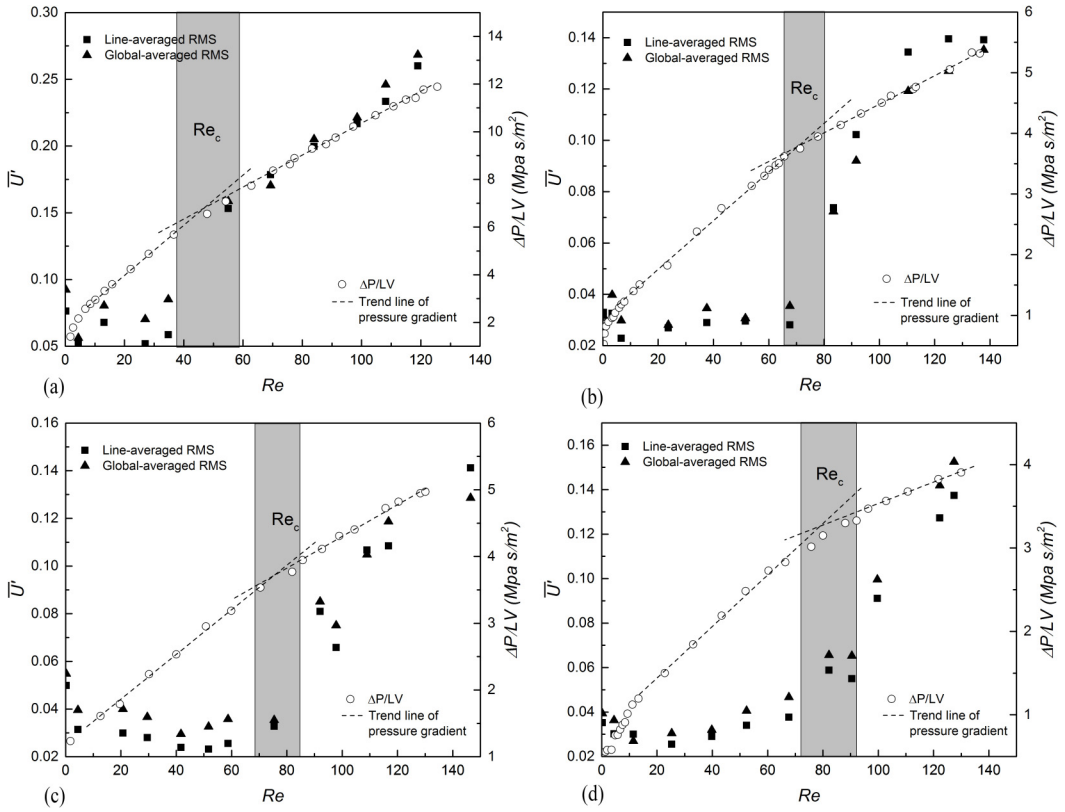

FIG. 8. Global averaged velocity fluctuation (left-hand y axis) versus Reynolds number for various porosities. Trend lines of pressure gradient in Forchheimer and turbulent regimes are drawn with a dashed line to find out the critical Reynolds number (Re_c). The critical area is filled with grey color. (a) Sample F72, (b) sample F77, (c) sample F78, and (d) sample F81.

near the wall as discussed above. This is due to the extreme complexity of the geometry in all three dimensions.

By examining the variation of turbulence intensity with Re, the critical Reynolds number (Re_c) between the laminar and turbulent flow can be obtained. Figure 8 shows the global averaged velocity fluctuation versus Reynolds number for porous media with different porosities. The value was calculated by averaging the local normalized velocity fluctuation over a line or the whole valid 2D region, represented as $\overline{U'}$. To compare to the critical Reynolds number obtained from pressure measurements, the pressure gradient data are also presented in the same plot (right-hand y axis). The trend of pressure gradient data in Forchheimer and turbulent flow regimes were fitted respectively, and the intersection region is where the critical point locates. As the transition point cannot be identified as a single point but a quite wide region, a grey band is used to highlight the transition region. The plots show that the critical Reynolds number obtained from pressure gradient measurements agrees very well with that obtained in μ-PIV measurement. This critical number identifies the transition from laminar to turbulent flow, because in all samples, the velocity fluctuation keeps at a nearly fixed, low value at Re below Re_c, and increases dramatically at Re just above Re_c. Although there is a similar trend of the turbulence intensity with Re in all samples, the difference in fluctuation intensities is also apparent. For example, the low porosity sample (F72) shows an overall higher fluctuation level; i.e., when $\mathrm{Re} = 120$, the fluctuation intensity in F72 is about 0.25, which is two times higher than other samples.

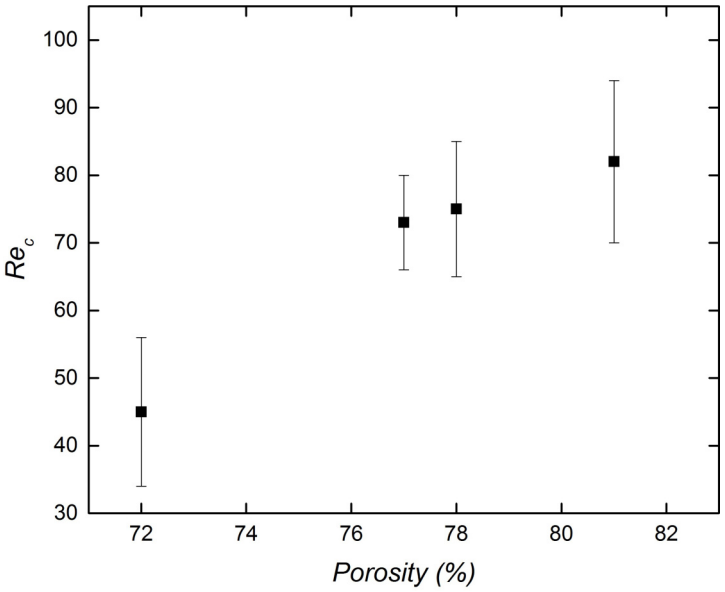

FIG. 9. Variation of critical Reynolds number with porosity.

C. Critical Reynolds numbers

The critical Reynolds numbers obtained from Figs. 8(a)–8(d) are plotted versus porosity in Fig. 9. Although only a limited range and number of porosities have been tested, the trend that the critical Reynolds number increases with porosity is still apparent. Since μ-PIV measurement cannot effectively identify the transition point between pre-Darcy, Darcy, and Forchheimer flow, the boundaries of the flow regimes obtained from the pressure gradient measurements are compared to what is available in the literature, which is shown in Table III. Unfortunately, only limited similar porous media are available. Both Fand *et al.* [1] and Kececioglu and Jiang [2] used packed glass spheres as the study object and included points from the Darcy regime to the turbulent regime. For packed spheres, sphere diameter was used as the characteristic length in calculating Reynolds number, while in the present study, pore diameter was used. Kececioglu and Jiang [2] used two different sphere sizes for measurements, which resulted in smaller Re for all regime boundaries compared with ours. This disagreement may be caused by the porosity, internal structure, and characteristic length differences, because if the results of the 3-mm and 6-mm spheres are compared, the Reynolds number seems to be only affected by sphere size (all critical Re with 6-mm spheres are about twice that with 3-mm spheres). However, when Fand *et al.* [1] mixed different sized spheres together, the results were different from that of Kececioglu and Jiang [2].

The literature on fluid flow in metal foam porous media also contains disagreement regarding transitions among flow regimes and flow regime boundaries [3]. Boomsma and Poulikakos [3] only provided the transition velocity and the pore size based transition Reynolds number between the Darcy and Forchheimer flow regimes, and the transition Reynolds number is quite high compared with the packed sphere porous media or the present materials, probably due to the high porosity and different structure.

V. CONCLUSIONS

In this paper, open cell microscale porous media are fabricated using a pore forming agent removal method and then experimentally tested to evaluate their hydraulic characteristics. Four porous samples with porosities of 72%, 77%, 78%, and 81% were characterized using both

TABLE III. Flow regime boundaries of current and previous studies. PPI-pores per inch.

	Materials	pre-Darcy	Darcy	Forchheimer	Turbulent
Current study	F72	$\mathrm{Re} < 3.50(\pm 0.25)$	$3.50(\pm 0.25) < \mathrm{Re} < 4.8(\pm 0.5)$	$6.8(\pm 0.5) < \mathrm{Re} < 47(\pm 6)$	$62(\pm 6) < \mathrm{Re}$
	F77	$\mathrm{Re} < 1.72(\pm 0.25)$	$1.72(\pm 0.25) < \mathrm{Re} < 4.5(\pm 0.5)$	$8.8(\pm 0.5) < \mathrm{Re} < 65(\pm 6)$	$71(\pm 6) < \mathrm{Re}$
	F78	$\mathrm{Re} < 1.55(\pm 0.25)$	$1.55(\pm 0.25) < \mathrm{Re} < 3.7(\pm 0.5)$	$10.0(\pm 0.5) < \mathrm{Re} < 70(\pm 6)$	$70(\pm 6) < \mathrm{Re}$
	F81	$\mathrm{Re} < 1.34(\pm 0.25)$	$1.34(\pm 0.25) < \mathrm{Re} < 2.7(\pm 0.5)$	$11.1(\pm 0.5) < \mathrm{Re} < 75(\pm 6)$	$88(\pm 6) < \mathrm{Re}$
Fand *et al.* [1], water	Packed spheres (35%)	NA	$\mathrm{Re} < 2.3(\pm 0.1)$	$5.0(\pm 0.5) < \mathrm{Re}_k < 80(\pm 5)$	$120 < \mathrm{Re}$
Kececioglu and Jiang	3-mm sphere (40%)	$\mathrm{Re} < 0.30(\pm 0.02)$	$0.30(\pm 0.02) < \mathrm{Re} < 0.70(\pm 0.05)$	$1.6(\pm 0.3) < \mathrm{Re} < 10(\pm 0.5)$	$13(\pm 1) < \mathrm{Re}$
	6-mm sphere (40%)	$\mathrm{Re} < 0.60(\pm 0.02)$	$0.60(\pm 0.02) < \mathrm{Re} < 1.00(\pm 0.03)$	$3.0(\pm 0.3) < \mathrm{Re} < 21(\pm 1)$	$25(\pm 1) < \mathrm{Re}$
Boomsma and Poulikakos [3], water	10 PPI (92.1%)	NA	$\mathrm{Re} < 725$	$725 < \mathrm{Re}$	NA
	20 PPI (92%)	NA	$\mathrm{Re} < 412$	$412 < \mathrm{Re}$	NA
	40 PPI (92.8%)	NA	$\mathrm{Re} < 177$	$177 < \mathrm{Re}$	NA

pressure-drop measurements and μ-PIV measurements. The Reynolds number range studied was approximately from 0.1 to 140.

Using pressure-drop measurements, four different Reynolds number regimes, identified as pre-Darcy, Darcy, Forchheimer, and turbulent, were identified as the flow rate through the porous media was increased. It is found that the pressure drop depends significantly on porosity and shows a linear relationship with Reynolds number in the Darcy regime and a nonlinear relationship in other regimes. It is also verified that the permeability of porous media is affected by the flow behavior and changes when using different regimes for calculation. Darcy permeability reflects the effect of internal porous structure alone, so it may be used to compare the permeability of different porous media. To characterize the flow resistance, however, the flow regime must be specified and both permeability and form drag coefficient need to be stated.

The μ-PIV measurements allow us to get an insight into the velocity and fluctuation distribution in pores of microporous media. Despite the considerable complexity of the pore space, the velocity profile shows a parabolic shape in the pre-Darcy and Darcy regimes, and becomes much fuller in the turbulent regime. PIV measurements have verified that the pre-Darcy and Darcy flows are steady laminar flow, followed by the unsteady laminar flow (Forchheimer regime), and then highly unsteady and chaotic flow (turbulent regime). The flow visualizations obtained from μ-PIV demonstrated that, as the Reynolds number varies, different routes become effective at transporting fluid in the porous media and the flow path changes significantly. This corresponds to the different flow regimes, each having a different effective permeability due to these changes in flow path. The μ-PIV measurements also allowed the quantification of the velocity fluctuations that characterize the unsteady flow. As such the critical Reynolds number could be identified at the transition between laminar and turbulent flow. This compared very well with the critical Re between the Forchheimer and turbulent flow regimes identified from the pressure-drop measurements.

Regarding the techniques used in this paper, the two methods work very well together and they provide an effective way to study the flow regime changes in microporous media. The μ-PIV method can be used to extract detailed information on the local flow behavior and could be valuable in studying flow effects in more complex porous structure analogs, for example, bimodal pore distributions or graded porosity structures. The understanding of the flow behavior in microporous media also provides a possible insight into the potential heat transfer performance of porous materials under forced convection and could inspire a new direction in designing porous structures for thermal applications.

ACKNOWLEDGMENTS

This work has been supported by the Engineering and Physical Sciences Research Council (Grant No. EP/N006550/1). X.K.L. would like to thank the University of Liverpool and the Chinese Scholarship Council for a studentship.

[1] R. M. Fand, B. Y. K. Kim, A. C. C. Lam, and R. T. Phan, Resistance to the flow of fluids through simple and complex porous media whose matrices are composed of randomly packed spheres, J. Fluids Eng. **109**, 268 (1987).

[2] I. Kececioglu and Y. Jiang, Flow through porous media of packed spheres saturated with water, J. Fluids Eng. **116**, 164 (1994).

[3] K. Boomsma and D. Poulikakos, The effects of compression and pore size variations on the liquid flow characteristics in metal foams, J. Fluids Eng. **124**, 263 (2002).

[4] S. Y. Kim, J. W. Paek, and B. H. Kang, Flow and heat transfer correlations for porous fin in a plate-fin heat exchanger, J. Heat Transfer **122**, 572 (2000).

[5] N. Dukhan, Ö. Bağcı, and M. Özdemir, Metal foam hydrodynamics: Flow regimes from pre-Darcy to turbulent, Int. J. Heat Mass Transfer **77**, 114 (2014).

[6] A. Koekemoer and A. Luckos, Effect of material type and particle size distribution on pressure drop in packed beds of large particles: Extending the Ergun equation, Fuel **158**, 232 (2015).
[7] K. G. Allen, T. W. Von Backström, and D. G. Kröger, Packed bed pressure drop dependence on particle shape, size distribution, packing arrangement and roughness, Powder Technol. **246**, 590 (2013).
[8] H. Darcy, Les fontaines publique de la ville de dijon, Dalmont, Paris **647**, 560 (1856).
[9] P. Forchheimer, Water movement through the ground, Zeitz. Ver. Duetch Ing. **45**, 1781 (1901).
[10] A. Dybbs and R. V. Edwards, A new look at porous media fluid mechanics: Darcy to turbulent, in *Fundamentals of Transport Phenomena in Porous Media* (Springer, Berlin, 1984), pp. 199–256.
[11] J. Bear, *Dynamics of Fluids in Porous Media* (Elsevier, New York, 1972).
[12] D. A. Nield and A. V. Kuznetsov, An historical and topical note on convection in porous media, J. Heat Transfer **135**, 061201 (2013).
[13] J. W. Foreman, Jr., E. W. George, and R. D. Lewis, Measurement of localized flow velocities in gases with a laser Doppler flowmeter, Appl. Phys. Lett. **7**, 77 (1965).
[14] W. Johnston, A. Dybbs, and R. Edwards, Measurement of fluid velocity inside porous media with a laser anemometer, Phys. Fluids **18**, 913 (1975).
[15] L. M. Peurrung, M. Rashidi, and T. J. Kulp, Measurement of porous medium velocity fields and their volumetric averaging characteristics using particle tracking velocimetry, Chem. Eng. Sci. **50**, 2243 (1995).
[16] A. Y. L. Huang, M. Y. F. Huang, H. Capart, and R.-H. Chen, Optical measurements of pore geometry and fluid velocity in a bed of irregularly packed spheres, Exp. Fluids **45**, 309 (2008).
[17] M. Raffel *et al.*, *Particle Image Velocimetry: A Practical Guide* (Springer, Heidelberg, 2007).
[18] S. Saleh, J. F. Thovert, and P. M. Adler, Measurement of two-dimensional velocity fields in porous media by particle image displacement velocimetry, Exp. Fluids **12**, 210 (1992).
[19] M. A. Northrup, T. J. Kulp, S. M. Angel, and G. F. Pinder, Direct measurement of interstitial velocity field variations in a porous medium using fluorescent-particle image velocimetry, Chem. Eng. Sci. **48**, 13 (1993).
[20] J. G. Santiago, S. T. Wereley, C. D. Meinhart, D. J. Beebe, and R. J. Adrian, A particle image velocimetry system for microfluidics, Exp. Fluids **25**, 316 (1998).
[21] C. D. Meinhart, S. T. Wereley, and J. G. Santiago, PIV measurements of a microchannel flow, Exp. Fluids **27**, 414 (1999).
[22] B. Zerai, B. Z. Saylor, J. R. Kadambi, M. J. Oliver, A. R. Mazaheri, G. Ahmadi, G. S. Bromhal, and D. H. Smith, Flow characterization through a network cell using particle image velocimetry, Transp. Porous Media **60**, 159 (2005).
[23] D. Sen, D. S. Nobes, and S. K. Mitra, Optical measurement of pore scale velocity field inside microporous media, Microfluid. Nanofluid. **12**, 189 (2012).
[24] Y. Y. Zhao and D. X. Sun, A novel sintering-dissolution process for manufacturing Al foams, Scr. Mater. **44**, 105 (2001).
[25] L. S. Han, Hydrodynamic entrance lengths for incompressible laminar flow in rectangular ducts, J. Appl. Mech. **27**, 403 (1960).
[26] R. J. Goldstein and D. K. Kreid, Measurement of laminar flow development in a square duct using a laser-Doppler flowmeter, J. Appl. Mech. **34**, 813 (1967).
[27] K. Bai and J. Katz, On the refractive index of sodium iodide solutions for index matching in PIV, Exp. Fluids **55**, 1704 (2014).
[28] R. Lindken, M. Rossi, S. Große, and J. Westerweel, Micro-particle image velocimetry (μPIV): Recent developments, applications, and guidelines, Lab Chip **9**, 2551 (2009).
[29] P. I. Polubarinova-Koch, *Theory of Ground Water Movement* (Princeton University Press, Princeton, NJ, 2015).
[30] D. Swartzendruber, Non-Darcy flow behavior in liquid-saturated porous media, J. Geophys. Res. **67**, 5205 (1962).

[31] B. V. Antohe, J. L. Lage, D. C. Price, and R. M. Weber, Experimental determination of permeability and inertia coefficients of mechanically compressed aluminum porous matrices, J. Fluids Eng. **119**, 404 (1997).

[32] W. Zhong, X. Li, F. Liu, G. Tao, B. Lu, and T. Kagawa, Measurement and correlation of pressure drop characteristics for air flow through sintered metal porous media, Transp. Porous Media **101**, 53 (2014).

[33] S. Mancin, C. Zilio, A. Cavallini, and L. Rossetto, Pressure drop during air flow in aluminum foams, Int. J. Heat Mass Transfer **53**, 3121 (2010).